Journal of Non-Crystalline Solids 515 (2019) 133–142

Contents lists available at ScienceDirect

Journal of Non-Crystalline Solids

journal homepage: www.elsevier.com/locate/jnoncrysol

Balance between accuracy and simplicity in empirical forcefields for glass modeling: Insights from machine learning

Han Liu[a], Zipeng Fu[a,b], Yipeng Li[a], Nazreen Farina Ahmad Sabri[a], Mathieu Bauchy[a,*]

[a] Physics of AmoRphous and Inorganic Solids Laboratory (PARISlab), Department of Civil and Environmental Engineering, University of California, Los Angeles, CA 90095, USA

[b] Department of Computer Science, University of California, Los Angeles, CA 90095, USA

ARTICLE INFO

Keywords:
Interatomic potential
Molecular dynamics simulation
Bayesian optimization

ABSTRACT

Classical molecular dynamics and Monte Carlo simulations of glassy materials critically rely on the availability of accurate empirical forcefields. To this end, empirical forcefields must exhibit an optimal balance between accuracy and simplicity—wherein forcefields that are too simple (underfitted) may not offer accurate predictions, whereas those that are too complex (overfitted) may not provide a good transferability over various systems. However, the development of new forcefields that capture the essential features of glassy materials while retaining minimum complexity has largely remained intuition-based thus far. Here, we report a new forcefield parametrization method that is based on machine learning optimization. By taking the example of glassy silica, we show that this approach allows us to identify the optimal degree of forcefield complexity in a non-biased fashion. Our method could greatly accelerate the development of new accurate, yet transferable forcefields for the modeling of silicate glasses.

1. Introduction

The development of accurate, yet transferable empirical forcefields is key to model multicomponent glasses by molecular dynamics (MD) or Monte Carlo simulations [1,2]. To this end, several forms of empirical potentials are available, ranging from very simple (e.g., Lennard Jones potential) to very complex (e.g., ReaxFF potential [3–5]). The degree of complexity of empirical forcefields mostly depends on the number of parameters that need to be parameterized, which can range from 2 (for Lennard Jones potentials) to hundreds (for ReaxFF) of parameters for pairs of elements. As such, the parameterization of a new forcefield typically follows two steps: (i) selecting an appropriate analytical form and degree of complexity and (ii) optimizing the value of the forcefield parameters [2,6,7].

The second step has been extensively addressed, as several methods have been proposed to optimize the parameters of a given forcefield formulation to properly describe the structure and properties of a given system. The parameterization of a forcefield can usually be described as an optimization problem, wherein a given cost function needs to be minimized. On the one hand, the cost function can be defined based on the difference between the structure or properties of simulated and experimental glasses. However, this approach can be problematic as the cooling rates used in MD simulations and experiments are dramatically different, which renders challenging a meaningful comparison between simulated and experimental glasses [8–10]. On the other hand, for a given system, the cost function can be defined based on the difference between the outcomes of classical and ab initio molecular dynamics (AIMD) simulations [11–13]. Kob, Huang et al. have recently proposed a new forcefield parameterization strategy that consists in defining the cost function in terms of the difference between the pair distribution function of a liquid simulated by AIMD and classical MD (i.e., as predicted by the forcefield that is to be trained) [11,14,15]. However, this cost function is very "rough," that is, it exhibits many local minima—i.e., the parametrization can yield several forcefields with different parameters, yet competitive accuracy [11,15]. As such, the outcome of the parameterization strongly depends on the starting point that is used [16]—so that the parameterization of the potential requires some level of "intuition."

In contrast, the first step of forcefield parameterization (i.e., selecting an appropriate degree of complexity) has received very little attention and often remains entirely based on "intuition" or "previous experience." However, selecting the right level of complexity is key to obtain accurate, yet transferable potentials. In details, forcefields that are too simple may not properly describe complex systems—for instance, Lennard Jones only rely on two parameters and, hence, are usually unable to properly predict at the same time the molar volume,

* Corresponding author.
E-mail address: bauchy@ucla.edu (M. Bauchy).

https://doi.org/10.1016/j.jnoncrysol.2019.04.020
Received 29 January 2019; Received in revised form 4 April 2019; Accepted 17 April 2019

molar energy, and stiffness of even simple systems (e.g., perfect gas). In contrast, forcefields that are too complex may offer an extremely accurate description of a targeted system, but offer very poor predictions when applied to systems that were not explicitly accounted for during the training of the forcefield (i.e., low transferability to new systems). In general, this competition between accuracy, transferability, and simplicity is known as a balance between "underfitting" and "overfitting."

Here, we report a new forcefield parametrization method that is based on machine learning (ML), which aims to reduce/suppress the need for intuition when (i) selecting the appropriate level of complexity for a forcefield and (ii) optimizing the value of the forcefield parameters. To illustrate this method, we take the examples of glassy silica as a system and of a Buckingham formulation for the forcefield. Our method allows us to quickly and robustly identify some optimal forcefield parameters for different degrees of forcefield complexity and, based on these results, to identify the optimal balance between forcefield accuracy and simplicity. Overall, our method could greatly accelerate the development of new accurate, yet transferable forcefield for the modeling of silicate glasses.

This paper is organized as follows. First, Section 2 describes the forcefield formulation (and complexity thereof) that is adopted herein and offers a detailed description of our ML-based parameterization strategy. We then investigate the influence of the forcefield complexity in Section 3. Finally, some conclusions are given in Section 4.

2. Methods

2.1. Empirical forcefields of different complexity

Glassy silica (g-SiO_2) is an archetypal ionocovalent system—whose interatomic potential energy can be well described by the Buckingham form relying only on two-body interactions between each pair of atom i, j [6,11,12]:

$$U_{ij} = \frac{q_i q_j}{4\pi\varepsilon_0 r_{ij}} + A_{ij}\exp\left(-\frac{r_{ij}}{\rho_{ij}}\right) - \frac{C_{ij}}{r_{ij}^6} + \frac{D_{ij}}{r_{ij}^{24}} \quad (1)$$

where r_{ij} is the distance between each pair of atoms, q_i are the partial charges of each atom (q_O for oxygen, q_{Si} for silicon, so that $q_O = -q_{Si}/2$), ε_0 is the dielectric constant, and the parameters A_{ij}, ρ_{ij}, C_{ij}, and D_{ij} describe the short-range interactions. A cutoff of 8 Å is here consistently used for the short-range interactions. The long-range coulombic interactions are evaluated by damped shifted force (dsf) model [17] with a damping parameter of 0.25 and a cutoff of 8 Å. Here, the last term is added as a strong repulsion at short-distance to avoid the "Buckingham catastrophe" [11], wherein the D_{ij} parameter is fixed to prevent any atomic overlap based on Ref. [11] (viz., $D_{ij} = 113$, 29, and 3,423,200 eV·Å^{24} for O—O, Si—O, and Si—Si interactions, respectively). In total, 10 independent parameters need to be parameterized for this forcefield formulation (Eq. (1)), namely, the partial charge q_{Si} and the short-range parameters $\{A_{ij}, \rho_{ij}, C_{ij}\}$ for each of the three atomic pairs (Si—O, O—O, and Si—Si). This set of parameters is denoted Ξ thereafter.

In the present case, the degree of complexity of this forcefield can be quantified by the number of parameters that are non-zero (out of the 10 independent parameters). For instance, although they are both based on the same Buckingham formulation, the well-established van Beest–Kramer–van Santen (BKS) [12] potential does not comprise any Si—Si energy terms, whereas such terms are present within the Carré–Horbach–Ipsas–Kob (CHIK) potential [11]. Here, to assess the influence of the potential complexity, we parameterize via a novel ML approach three potentials featuring an increasing level of complexity, namely (i) ML-SiO, wherein only Si—O interaction energy terms are considered (i.e., 4 non-zero parameters in Ξ), (ii) ML, wherein only Si—O and O—O interaction energy terms are considered (i.e., 7 non-zero parameters in Ξ), and (iii) ML-ALL, wherein all the Si—O, O—O, and Si—Si interaction energy terms are considered (i.e., 10 non-zero parameters in Ξ).

2.2. Forcefield parameterization from ab initio simulation

Following Kob and Huang et al., the determination of the optimal parameters Ξ is conducted by minimizing the difference between the outcomes of classical MD and AIMD while simulating an equilibrium silica liquid [11,14,15]. To this end, we define the cost function R_χ as follows:

$$R_\chi = \sqrt{\frac{\chi_{SiO}^2 + \chi_{OO}^2 + \chi_{SiSi}^2}{3}} \quad (2)$$

where the ${\chi_{\alpha\beta}}^2$ terms capture the level of agreement between the partial pair distribution functions (PDFs) obtained by classical MD and AIMD [18]:

$$\chi_{\alpha\beta}^2 = \frac{\sum_r [g_{\alpha\beta}^{AIMD}(r) - g_{\alpha\beta}^{MD}(r)]^2}{\sum_r [g_{\alpha\beta}^{AIMD}(r)]^2} \quad (3)$$

where ${g_{\alpha\beta}}^{AIMD}(r)$ and ${g_{\alpha\beta}}^{MD}(r)$ are the partial PDFs for each pair of atoms α–β. Note that, among potential alternative structural metric describing the structure of the simulated glasses or liquids, the PDF offers a convenient description of the short-range environment around each atom [11,14,19]. We purposely exclude from the training set any of the properties of glassy SiO_2 (e.g., experimental density or stiffness) as such properties are not uniquely defined and depend on the cooling rate. This training scheme is motivated by the fact that Buckingham-type potentials have been shown to properly describe (i) the temperature-dependence of glass and liquid properties and (ii) the dependence of glass properties on the cooling rate (see Refs. [8–10]), so that training the system for a fixed temperature should yield a good description of its behavior as a function of temperature, including in the glassy state. A similar approach was used in Refs. [11, 14]. The technical details of MD and AIMD simulations are provided below.

2.2.1. Reference AIMD simulations

The "reference" liquid silica structure is prepared by Car-Parrinello molecular dynamics (CPMD) [20]. 38 SiO_2 units (114 atoms) are placed within a periodic cubic simulation box of length 11.982 Å to match the experimental density of 2.2 g/cm^3 [21]. The electronic structure of the atoms is described within the framework of density functional theory. The choice of pseudopotentials for each atom-type, exchange and correlation functions, and the plane-wave cutoff (70 Ry) are based on previous CPMD simulations of glassy silica [11,14]. A timestep of 0.0725 fs and a fictitious electronic mass of 600 a.u. are used. A liquid configuration obtained by classical MD simulation at 3600 K using the well-established BKS potential is used an initial configuration (see Section 2.1) [12]. This configuration is then relaxed via CPMD at 3600 K and constant volume for 3.5 ps—which duration is long enough due to the small relaxation time of the system at such elevated temperature. A subsequent dynamics of 16 ps is then used for statistical averaging and to compute the Si—Si, Si—O, and O—O PDFs of the simulated liquid system. Note that, although certain properties strongly depend on the system size (e.g., ring size distribution, vibrational properties, transport properties, etc.), partial PDFs have been shown to be fairly unaffected by the system size (as long as it is larger than 100 atoms, see Refs. [13, 22]). More details on the CPMD simulations can be found in Ref. [11, 14].

2.2.2. Classical MD simulation

For each set of forcefield parameters Ξ considered herein, we conduct a classical MD simulation of the same liquid silica system. The simulated system comprises 1000 SiO_2 units (3000 atoms) placed in a periodic cubic simulation box of length 35.661 Å—in accordance with the experimental density of 2.2 g/cm^3 [21]. The configuration is first

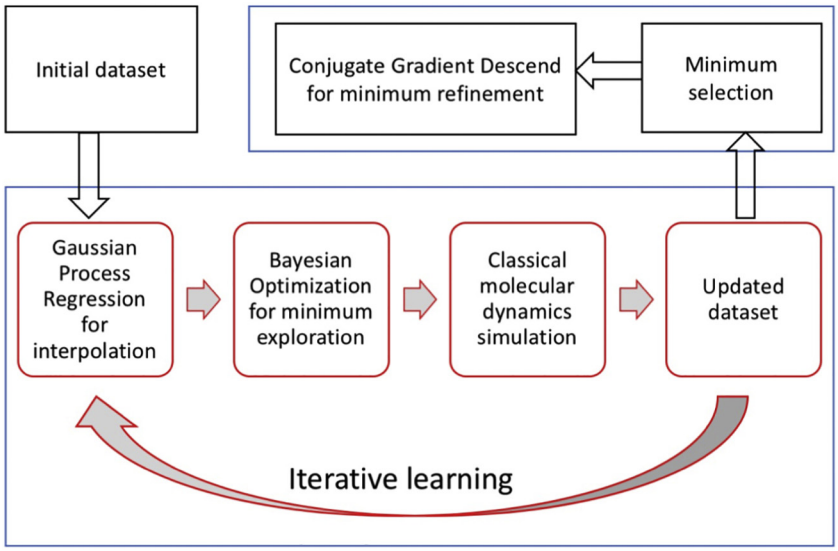

Fig. 1. Flow-chart of the machine-learning-based parametrization strategy proposed herein.

fully relaxed for 10 ps at 3600 K in the *NVT* ensemble. The partial PDFs of the simulated systems are then computed based on statistical averaging in a subsequent *NVT* dynamics of 10 ps. A timestep of 1 fs is consistently used for all simulations.

2.3. Machine learning forcefield optimization

We now introduce the ML-based optimization scheme that is used to minimize the cost function and, thereby, parametrize the three forcefields considered herein (i.e., with different level of complexity). Fig. 1 shows an overview of the parametrization process. First, we construct an initial dataset containing some "known points," that is, the values of the cost function R_χ for select sets of parameters Ξ. This dataset serves as a training set for the machine learning algorithm, which is able to "learn by example" the relationship between the parameters Ξ and the cost function R_χ. To this end, we use Gaussian Process Regression (GPR) [23,24] to interpolate the known points (and assess the uncertainty of the interpolation) over the entire parameter space. The Bayesian Optimization (BO) method [23] is then used to analyze the interpolated function and its uncertainty in order to predict an optimal set of parameters Ξ—which offers the best "exploration vs. exploitation tradeoff", that is, the best balance between (i) exploring the parameter space and reducing the model uncertainty and (ii) exploiting the present apparent minimum and finding the global minimum of the cost function. The "true" cost function $R_\chi\{\Xi\}$ associated with the set of parameters predicted by BO is subsequently calculated by conducting a classical MD simulation and comparing the simulated structure with the reference AIMD configuration (see Section 2.2). This new datapoint $R_\chi\{\Xi\}$ is then added to the dataset. The new dataset is then used to refine the GPR-based interpolation and predict a new optimal set of parameters by BO. This cycle is iteratively repeated until a satisfactory minimum in the cost function is obtained, that is, when R_χ does not decrease any further. Finally, the global minimum predicted by BO is further refined by conducting a conjugate gradient (CG) optimization [16]. Each of these steps is further described in the following.

2.3.1. Initial dataset

As a starting point for our optimization method, we construct an initial dataset, which contains as inputs a selection of potential parameters Ξ and as outputs the associated cost function R_χ. Each of these datapoints is obtained by an independent MD simulation (see Section 2.2). This initial dataset offers an ensemble of known values for the cost function in 10-dimensional parameter space (i.e., for the 10 components in Ξ), which is used as a starting point for the iterative interpolation/exploration process described in the following. These initial values of Ξ are chosen so as to uniformly span the targeted range of parameters (chosen based on previously available forcefield). In the case of wide target ranges, we divide the target range into several small pitches for fast exploration. The initial dataset comprises about 1000 known points, which corresponds to a minuscule fraction of the parameter space. For instance, with 10 independent parameters, considering only two values for each parameter would yield $2^{10} = 1024$ possible combinations. Each known point is obtained by conducting an MD simulation that takes about 1 min of computation using 16 CPU cores. Overall, it takes about 17 h to establish the initial dataset.

2.3.2. Interpolation by Gaussian Process Regression

The basic principle of GPR is to infer the (Gaussian-type) probability distribution of the values of the function that is interpolated based on a set of known points [23,24]. The interpolation process follows the following expression:

$$P(R_\chi(\Xi^*)|\{R_\chi(\Xi_{known})\}) \Longleftarrow \begin{bmatrix} R_\chi(\Xi_1) \\ \vdots \\ R_\chi(\Xi_n) \\ R_\chi(\Xi^*) \end{bmatrix} \sim \text{Normal}\left(\begin{bmatrix} \mu_0(\Xi_1) \\ \vdots \\ \mu_0(\Xi_n) \\ \mu_0(\Xi^*) \end{bmatrix}, \begin{bmatrix} \Sigma_0(\Xi_1,\Xi_1) & \cdots & \Sigma_0(\Xi_1,\Xi_n) & \Sigma_0(\Xi_1,\Xi^*) \\ \vdots & \ddots & \vdots & \vdots \\ \Sigma_0(\Xi_n,\Xi_1) & \cdots & \Sigma_0(\Xi_n,\Xi_n) & \Sigma_0(\Xi_n,\Xi^*) \\ \Sigma_0(\Xi^*,\Xi_1) & \cdots & \Sigma_0(\Xi^*,\Xi_n) & \Sigma_0(\Xi^*,\Xi^*) \end{bmatrix} \right) \quad (4)$$

where $P(R_\chi(\Xi^*)|\{R_\chi(\Xi_{known})\})$ is the conditional probability of the value of the cost function R_χ for a given set of parameters Ξ^* given the dataset of all the known points $\{R_\chi(\Xi_1),\ R_\chi(\Xi_2),\ \cdots\ R_\chi(\Xi_n)\}$, as denoted as $\{R_\chi(\Xi_{known})\}$. The conditional probability of $R_\chi(\Xi^*)$ is calculated using multivariate Gaussian distribution [25], where $\mu_0(\cdot)$ is the mean operation and $\Sigma_0(\cdot)$ is the covariance operation. There are many possible choices for the function-type of $\mu_0(\cdot)$ and $\Sigma_0(\cdot)$ and most can offer a reasonable extrapolation in the framework of multivariate Gaussian distribution [25]. Here, we adopt the Matern-type kernel for $\mu_0(\cdot)$ and $\Sigma_0(\cdot)$ [24,25]. In addition, to add some white-noise background during the interpolation [23], we also checked the intrinsic uncertainty of the cost function values yielded by the MD simulations by conducting a series of 10 independent MD simulations while keeping the same set of parameters Ξ and calculating the standard deviation of the associated

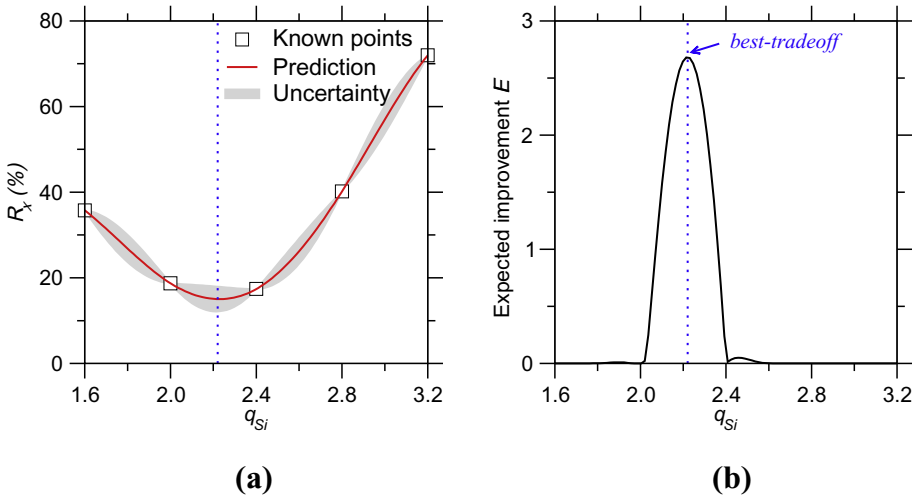

Fig. 2. Illustration of the Bayesian optimization approach used herein. Only the partial charge of the Si atoms q_{Si} is here optimized, while the other 9 forcefield parameters are kept fixed. **(a)** Interpolation of the cost function (R_χ, see Eq. (2)) offered by Gaussian Process Regression (red line) as a function of the q_{Si}. The prediction is based on an initial training set comprising 5 datapoints (i.e., known points, black symbols). The grey area indicates the uncertainty (95% confidence interval) of the prediction. **(b)** Expected Improvement (EI) function yielded by the Bayesian optimization method, which predicts the set of parameters (here, q_{Si}) that offers the best tradeoff between "exploration" (i.e., minimizing the uncertainty of the model presented in panel (a)) and "exploitation" (i.e., minimizing the cost function R_χ). (For interpretation of the references to colour in this figure legend, the reader is referred to the web version of this article.)

cost functions R_χ. We find that the computed cost function values have a relative uncertainty of about 2% when $R_\chi < 100\%$ (i.e., for realistic forcefields) and can increase up to 10% for higher values of R_χ (i.e., for fairly unrealistic forcefields). This level of noise is not expected to significantly affect the shape of interpolation around the minimum positions of the cost function R_χ.

Fig. 2(a) shows an example of the outcome of a GPR-based interpolation. For illustration purposes, only the partial charge of the Si atoms q_{Si} is here optimized, while the other 9 forcefield parameters are kept fixed and equal to those found in the original BKS potential [12]. A dataset comprising the values of the cost function R_χ for 5 values of q_{Si} ranging from 1.6-to-3.2 is first constructed. The interpolated function and the uncertainty thereof (95% confidence interval) predicted by GPR is shown in Fig. 2(a). As expected, we observe that the interpolated function exhibits a minimum with respect to q_{Si} (note that the q_{Si} value used in the BKS potential is 2.4). Unsurprisingly, the uncertainty of the prediction is low at the vicinity of the known points and increases in between them.

2.3.3. Minimum exploration by Bayesian optimization

Based on the interpolated function $R_\chi(\Xi)$ and uncertainty $\sigma(\Xi)$ thereof predicted by GPR, the BO method is used to determine the next optimal set of parameters Ξ to try based on an acquisition function that depends on $R_\chi(\Xi)$ and $\sigma(\Xi)$. Here, we adopt the expected improvement (EI) function, which is commonly used as acquisition function [23]:

$$\mathrm{EI}(\Xi) = \begin{cases} [R_\chi(\hat{\Xi}) - R_\chi(\Xi)]\Phi(Z) + \sigma(\Xi)\phi(Z) & \text{if } \sigma(\Xi) > 0 \\ 0 & \text{if } \sigma(\Xi) = 0 \end{cases} \quad (5)$$

where $Z = [R_\chi(\hat{\Xi}) - R_\chi(\Xi)]/\sigma(\Xi)$, $R_\chi(\hat{\Xi})$ is the current minimum value of R_χ among all the known points (in other words, $\hat{\Xi}$ is the current optimal set of parameters), and $\Phi(Z)$ and $\phi(Z)$ are the cumulative distribution and probability density function of the standard normal distribution, respectively. By construction, the value of $EI(\Xi)$ is high (i) when the expected value of $R_\chi(\Xi)$ is smaller than the current best value $R_\chi(\hat{\Xi})$ or (ii) when the uncertainty $\sigma(\Xi)$ around the point $\hat{\Xi}$ is high. Therefore, the maximum position of $EI(\Xi)$ indicates either a point for which a better minimum position of R_χ than the current one is expected or a point belonging to a region of R_χ that has not been explored yet (i.e., $\sigma(\Xi)$ is high). Namely, the maximum position of $EI(\Xi)$ offers the best tradeoff between "exploration" (i.e., minimizing the uncertainty $\sigma(\Xi)$) and "exploitation" (i.e., minimizing the cost function $R_\chi(\Xi)$).

As an illustration of the BO approach, Fig. 2(b) shows the computed expected improvement function based on the interpolated function and uncertainty thereof shown in Fig. 2(a). As mentioned above, only the partial charge of the Si atoms q_{Si} is here optimized, while the other 9 forcefield parameters are kept fixed and equal to those found in the original BKS potential [12]. As expected, we observe a noticeable maximum in the expected improvement function where the interpolated function R_χ is minimum (exploitation). Some secondary peaks are also observed in the high-uncertainty regions of the function in the vicinity of the minimum position.

2.3.4. Iterative refinement of the forcefield

Finally, at each step of our iterative optimization scheme, the set of parameters Ξ corresponding to the maximum of the expected improvement function is used to conduct an MD simulation and calculate the associated cost function value R_χ. In turn, this new datapoint is added to the dataset. This enhances the accuracy of the GPR interpolation, which contributes to further refine the sampling of the cost function R_χ at the vicinity of its minimum positions. This iterative scheme is repeated until convergence is achieved, that is, until the cost function reaches a plateau and does not further decrease within 100 iterations.

This iterative refinement method is illustrated in Fig. 3. Here, for illustrative purposes, only two parameters (q_{Si} and A_{SiO}) are optimized, while the other 8 forcefield parameters are kept fixed and equal to those found in the original BKS potential [12]. Fig. 3(a) shows a contour plot of the cost function R_χ as a function of the two free parameters used in the optimization. We observe that, even in the case of only two free parameters, the cost function shows a rough dependence on the parameters and exhibits two distinct minima (i.e., the dark blue domains in Fig. 3(a)). Fig. 3(a) also shows the pathway that is explored by the optimization algorithm in the (q_{Si}, A_{SiO}) space, that is, the set of parameters for which the expected improvement function is maximum after each step. We observe that the optimization quickly converges toward the global minimum of the cost function after only 5 iterations, after which the cost function R_χ shows a plateau around 10% (see Fig. 3(b)). This illustrates the efficiency of our optimization technique.

2.4. Final refinement by conjugate gradient (CG)

Finally, the minimum identified by the iterative BO scheme is further refined by the CG method. Indeed, although the BO method can quickly identify the vicinity of the global minimum of a rough function, the CG method is more efficient to pinpoint the minimum position in a local basin of the cost function. Here, we adopt the nonlinear CG algorithm detailed in Ref [16]. In short, we first use the secant method to construct a quadratic interpolation of $R_\chi(\Xi)$ at the vicinity of the minimum identified by the iterative BO scheme and determine the new minimum predicted by the CG interpolation. We then repeat the quadratic construction (i.e., the linear search) around this new

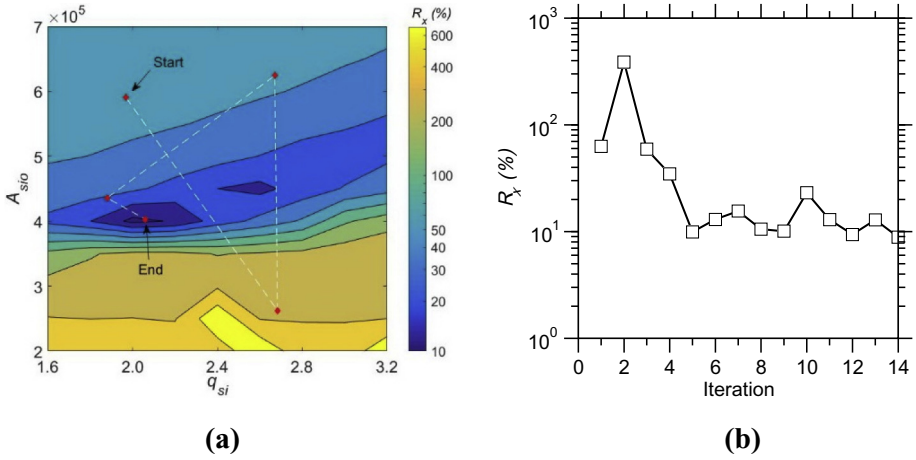

Fig. 3. Illustration of the iterative optimization approach used herein. Only the partial charge of the Si atoms q_{Si} and the parameter A_{SiO} are here optimized, while the other 8 forcefield parameters are kept fixed. **(a)** Contour plot showing the cost function R_χ as a function of q_{Si} and A_{SiO}. The white dashed line indicates the path explored by the Bayesian optimization method until the global minimum in the cost function R_χ is identified. **(b)** Evolution of the cost function R_χ of the best-tradeoff position predicted by the Bayesian optimization during the optimization process. (For interpretation of the references to color in this figure, the reader is referred to the web version of this article.)

minimum position. This is used to approximate the minimum position of R_χ along the CG direction (i.e., the search direction). The maximum number of iterations of linear search in a search direction is set as 3. Then, starting from the identified new minimum position, we calculate the local gradient and find a new search direction based on Polak-Ribiere formula [16]. A new search direction is then determined from this starting point to identify a new minimum position. The iterative scheme is repeated until convergence, that is, when the new minimum position largely overlaps with the last minimum position, R_χ shows a plateau, and the squared sum of the local gradient converges toward zero and remains lower than the "zero" threshold (taken as 5 herein) within 10 iterations.

Fig. 4 shows an illustration of the CG refinement step—starting from the minimum identified by the BO iterative scheme illustrated in Fig. 3. By exploring "downhill" the local minimum of the cost function (Fig. 4(a)), the CG allows us to further refine the position of the minimum—the cost function decreasing from 10% to about 9% (see Fig. 4(b)). As expected, the local gradient converges toward zero as the CG optimization proceeds (see Fig. 4(c)). Note that, due to the high roughness of the cost function, CG optimization alone cannot yield a satisfactory minimum for the cost function as it easily gets stuck in local minima [26].

3. Results

3.1. Accuracy of the forcefields

We now assess how the degree of complexity of the forcefield controls its accuracy. To this end, we compare the outcomes of our ML-based parametrization method for three forcefields featuring increasing degrees of complexity (see Section 2.1), namely, (i) ML-SiO, which only comprises Si−O energy terms, (ii) ML, which comprises Si−O and O−O energy terms (i.e., like the well-established BKS potential [12,27]), and (iii) ML-ALL, which comprises Si−O, O−O, and Si−Si energy terms (i.e., like the CHIK potential [11]). Note that, in all cases, the Coulombic interactions are computed for all the pairs of atoms—so that only the "Buckingham" contribution of these three potentials is varied. In order of increasing complexity, the three potentials comprise 4, 7, and 10 variable parameters, respectively (i.e., 3 parameters per interatomic pair and the Si partial charge). From a physical viewpoint, this analysis allows us (i) to investigate whether accounting for O−O interaction terms (i.e., besides the Coulombic repulsion) is truly necessary to predict a realistic structure for glassy silica and (ii) to assess the extent to which incorporating Si−Si energy terms can improve the performance of the forcefield. More generally, this analysis is conducted to identify the right level of complexity, that is, to develop a forcefield that is neither underfitted nor overfitted.

The parameters obtained for the ML potential are listed in Table 1,

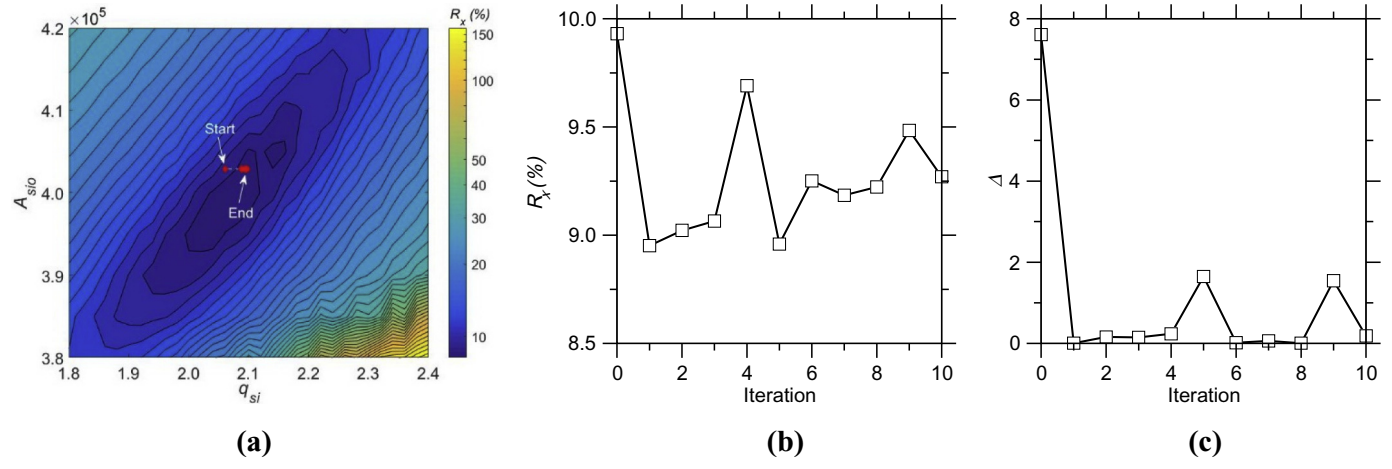

Fig. 4. Illustration of the final conjugate gradient optimization. Only the partial charge of the Si atoms q_{Si} and the parameter A_{SiO} are here optimized, while the other 8 forcefield parameters are kept fixed. **(a)** Contour plot showing the cost function R_χ as a function of q_{Si} and A_{SiO}. The white dashed line indicates the path explored by the conjugate gradient optimization method until the minimum in the cost function R_χ is identified. **(b)** Evolution of the cost function R_χ during the conjugate gradient optimization process. **(c)** Evolution of the squared-sum of the local gradient δ during the conjugate gradient optimization process.

Table 1
Parameters of the optimized potential "ML" (see Eq. (1)). The partial charges are indicated as superscripts for each pair of atoms.

Atomic pairs	$Si^{+1.955} - O^{-0.9775}$	$O^{-0.9775} - O^{-0.9775}$	$Si^{+1.955} - Si^{+1.955}$
A (eV)	20,453.6 ± 0.2	1003.4 ± 0.2	0
ρ (Å)	0.191735 ± 0.000005	0.356855 ± 0.000005	1
C (eV·Å^6)	93.5 ± 0.5	81.5 ± 0.5	0

Table 2
Parameters of the interatomic potential "ML-SiO" (which only considers Si—O interactions). The partial charges are indicated as superscripts for each pair of atoms.

Atomic pairs	$Si^{+1.484} - O^{-0.742}$	$O^{-0.742} - O^{-0.742}$	$Si^{+1.484} - Si^{+1.484}$
A (eV)	3968.5 ± 0.2	0	0
ρ (Å)	0.187600 ± 0.000005	1	1
C (eV·Å^6)	0.7 ± 0.5	0	0

whereas those obtained for the ML-SiO and ML-ALL potentials are listed in Tables 2 and 3. Overall, we find that the parameters of the ML-SiO forcefield significantly differ from those of the ML forcefield. In particular, we obtain a very small Si partial charge of +1.484. In contrast, we note that the parameters of the ML-ALL forcefield are largely similar to those of the ML potential—with a partial charge for Si atoms that is around 1.955. This value is fairly close to that of the CHIK (+1.91 [14]) and Wang–Bauchy potentials (+1.89 [6]).

Fig. 5 presents a comparison of the accuracy of the three forcefields (as quantified in terms of the final cost function R_χ). We note that the low-complexity ML-SiO potential offers a very poor description of the structure of silica (i.e., high final R_χ value—note that a threshold of 10% is typically used to discriminate "good" from "bad" forcefields [18]). This confirms that, as expected, the O—O interactions play a key role in predicting a realistic SiO_2 structure and that the ML-SiO model is clearly underfitted. In contrast, as shown in Fig. 5, the high-complexity ML-ALL potential offers a slight improvement in the description of the structure of silica with respect to that predicted by ML potential, which manifests itself by a slight decrease in R_χ from 8.77% to 7.20%. Although this improvement is higher than the level of uncertainty in the R_χ values, it remains small as compared to the difference between the R_χ values yielded by the ML and ML-SiO forcefields. This suggests that Si—Si interactions only play a minor role in controlling the structure of silica. In turn, this small improvement comes with a significantly higher degree of complexity (i.e., 3 extra parameters), which suggests that the ML-ALL potential may be overfitted.

3.2. Partial pair distribution functions

We now further investigate the effect of the complexity of the forcefield on the structure of the simulated liquid silica system (i.e., at 3600 K). To this end, Fig. 6 shows a comparison of the partial PDFs obtained by each of the three potentials. The data are compared with the reference ab initio partial PDFs used for the training of the potentials. We first focus on the ML potential (i.e., which exhibits the same level of complexity as the BKS potential). Overall, we find that the ML potential provides an excellent agreement with AIMD

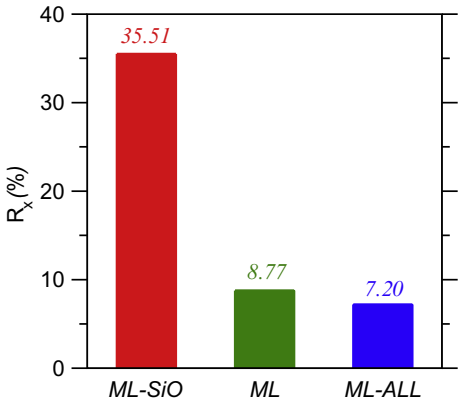

Fig. 5. Comparison of the final cost function values R_χ obtained by including, in order of increasing complexity: (i) only Si—O interactions ("ML-SiO" potential), (ii) both Si—O and O—O interactions ("ML" potential), and (iii) Si—O, O—O, and Si—Si interactions ("ML-ALL" potential). The relative uncertainty in the R_χ values is ± 0.5%, ± 0.25%, and ± 0.25% for the ML-SiO, ML, and ML-ALL forcefields, respectively.

simulations—although this is not surprising as our forcefield is specifically trained to match these data. Nevertheless, these results illustrate that the Buckingham formulation (see Eq. (1)) is adequate to describe the SiO_2 system. This result also further supports the ability of our ML-based optimization method to offer a robust parametrization. We note that the average Si—Si distance predicted by ML potential is slightly shifted compared with AIMD simulations (see Fig. 6(c)). This may arise from a general limitation of the Buckingham formulation.

We now focus on the low-complexity ML-SiO forcefield (which does not comprise O—O energy terms). Overall, we find that the ML-SiO forcefield exhibits a very unrealistic structure. Although this forcefield succeeds at predicting a reasonable average Si—O average interatomic distance (see Fig. 6(a)), it completely fails to properly model O—O correlations (see Fig. 6(b)). This confirms that including the O—O interactions is necessary to properly describe the tetrahedral structure of Si atoms and, hence, that the low-complexity ML-SiO forcefield is underfitted.

In contrast, we note that the structure predicted by the ML-ALL forcefield is largely similar to that offered by the ML potential, which confirms that Si—Si interactions play a fairly trivial role in controlling the structure of glassy SiO_2. Although we observe that taking into account Si—Si interactions offers a slight improvement in the Si—Si partial PDF, the average Si—Si distance remains overestimated with respect to that predicted by AIMD. This further suggests that this discrepancy is an intrinsic limitation of the two-body Buckingham formulation used herein. Although the inclusion of 3-body energy terms could overcome this limitation, this would come with a significant increase in computing cost and model complexity. Overall, these results confirm that the ML parametrization presented in Table 1 yields an excellent description of the structure of silica and offers the best balance between accuracy and model simplicity.

3.3. Partial bond angle distributions

We now investigate the effect of the forcefield complexity on the

Table 3
Parameters of the interatomic potential "ML-ALL" (which includes Si—Si interactions). The partial charges are indicated as superscripts for each pair of atoms.

Atomic pairs	$Si^{+1.955} - O^{-0.9775}$	$O^{-0.9775} - O^{-0.9775}$	$Si^{+1.955} - Si^{+1.955}$
A (eV)	20,453.6 ± 0.2	1003.4 ± 0.2	2643.1 ± 0.2
ρ (Å)	0.191735 ± 0.000005	0.356855 ± 0.000005	0.303616 ± 0.000005
C (eV·Å^6)	93.5 ± 0.5	81.5 ± 0.5	232.0 ± 0.5

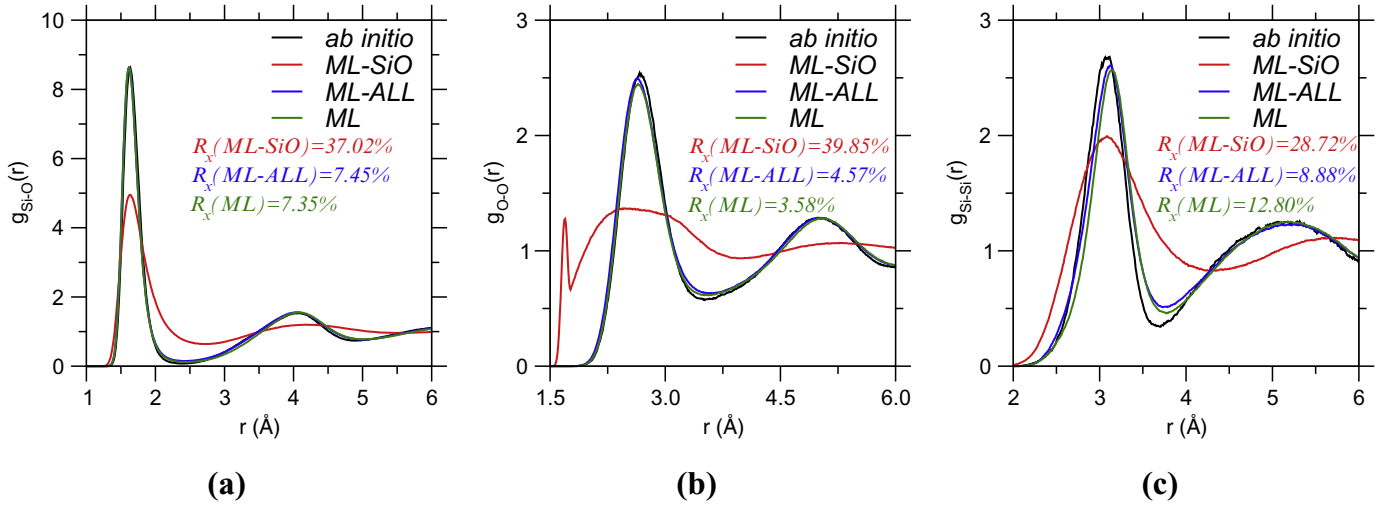

Fig. 6. (a) Si−O, **(b)** O−O, and **(c)** Si−Si partial pair distribution functions in liquid silica (at 3600 K) predicted by the different forcefields parameterized herein. The data are compared with the ab initio reference [14].

partial bond angle distributions (PBADs). Note that, the PBADs are not explicitly included in the cost function (see Eq. (2)) and that such 3-body correlations are not fully encoded in the 2-body correlations (i.e., as captured by the partial PDFs). As such, the PBADs allow us to assess the accuracy of the forcefield by comparing their predictions to a structural quantity that is unknown during the training of the forcefields. In that sense, the PBADs acts as a "test set," that is, a group of data that is deliberately kept invisible to the model during parametrization and can then be used to a posteriori assess the ability of the model to offer realistic predictions for unknown data. In addition, this analysis allows us to better understand the influence of the O−O and Si−Si interactions in controlling the angular environment of the Si and O atoms.

Fig. 7 shows the O−Si−O and Si−O−Si PBADs predicted by the three potentials for the liquid silica system (at T = 3600 K). The data are compared with those obtained by ab initio simulations [14]. We first focus on the ML potential (i.e., which exhibits the same level of complexity as the BKS potential). Overall, we observe that the PBADs predicted by the ML potential offer a very good agreement with ab initio simulations. As expected, the ML potential yields a tetrahedral environment for Si atoms (with an average O−Si−O angle of about 109°). Nevertheless, we observe that the ML potential slightly overestimates the value of Si−O−Si angles with respect to AIMD simulations, which appears to be a general limitation of the 2-body Buckingham formulation adopted herein and is likely related to the fact that our potential overestimates the Si−Si average distance (see Section 3.2).

We now focus on the low-complexity ML-SiO forcefield (which does not comprise O−O energy terms). We note that the ML-SiO potential (i) largely underestimates the average value of both the O−Si−O and Si−O−Si angles and (ii) overestimates the broadness of the angular distributions (i.e., the angular excursions) with respect to the AIMD simulations. These unrealistic PBADs offers a strong a posteriori validation of the fact that the ML-SiO potential is underfitted. In turn, these results demonstrate that explicitly accounting for the O−O interactions is essential to correctly model the tetrahedral structure of the Si atoms.

In contrast, we find that the PBADs predicted by the ML-ALL forcefield are fairly similar to those offered by the ML potential, which indicates that accounting for the Si−Si interactions may not be necessary to properly model the angular environment of the Si and O atoms. Further, a more detailed comparison of the PBADs predicted by the ML and ML-ALL potentials with the reference AIMD data reveals that the O−Si−O PBAD predicted by the ML potential is slightly better than that offered by the more complex ML-ALL potential (see Fig. 7(a)). Further, we note that, thanks to the addition of Si−Si energy terms, the ML-ALL offers a better description of the average value of the Si−O−Si angle. However, in turn, the Si−O−Si PBAD predicted by the ML-ALL potential exhibit a large degree of asymmetry that is not supported by the AIMD simulations (see Fig. 6(c)). This suggests that the fact of capturing all the fine details of the partial PDFs used during the training (as

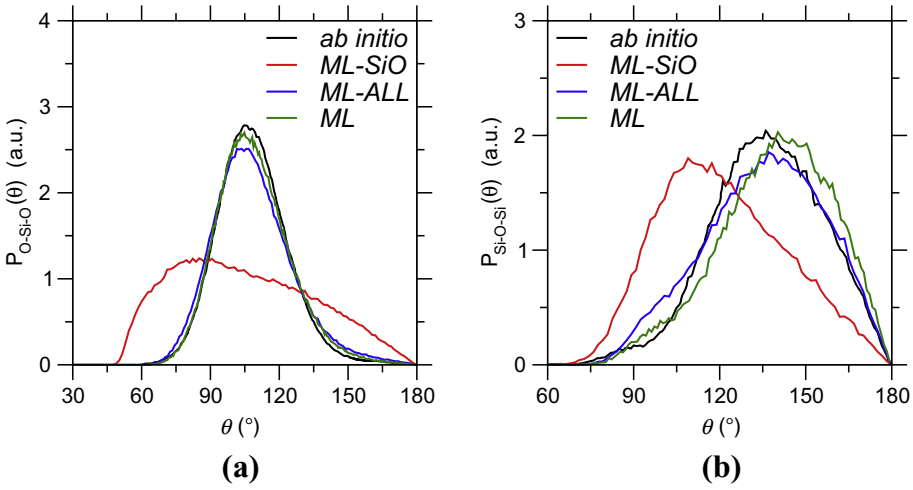

Fig. 7. (a) O−Si−O and **(b)** Si−O−Si partial bond angle distributions (PBADs) in liquid silica (at T = 3600 K) predicted by the different ML-based forcefields parameterized herein. The data are compared with the ab initio reference [14].

permitted by the high-complexity of the ML-ALL forcefield) results in some overfitting, which, in turn, manifests itself by a decrease in the ability of the potential to properly predict structural metrics that are not explicitly included in the training set. In contrast, due to its higher degree of simplicity, the ML potential only captures the essential features of the partials PDFs and, hence, offers more robust predictions for structural data that are kept invisible during training. This suggests that the ML potential (i.e., which relies on Si—O and O—O energy terms only) presents the best balance between under- and overfitting and, thereby, offers the most accurate overall description of the structure of glassy silica.

4. Discussion

4.1. Dependence on the initial training set

We now discuss the ability of our ML-based optimization scheme to yield a proper optimal set of forcefield parameters (i.e., to identify a proper minimum in the cost function) regardless of the choice of the initial training set, that is, the parameter space used as a starting point for the optimization (see Section 2.3). In particular, it is critical for the parameterization method to be able to yield a minimum in the cost function that is far from the initial training set. Indeed, this is key as we aim to develop a non-biased parameterization scheme that do not rely on "intuition" regarding the range of promising forcefield parameters.

Fig. 8 shows an illustration of the ability of our ML-based method to efficiently explore the parameter space—even far away from the initial training set—to yield a proper minimum in the cost function. Here, for illustrative purposes, only two parameters (q_{Si} and A_{SiO}) are optimized, while the other 8 forcefield parameters are kept fixed and equal to those found in the original BKS potential [12]. Fig. 8(a) shows a contour plot of the cost function R_χ as a function of the two free parameters used in the optimization. In this case, we purposely restrict the region of the initial training set to $q_{Si} > 2.4$ (i.e., the colored region in Fig. 8(a)), which does not comprise the targeted global minimum position of R_χ. We observe that our iterative learning model is able to quickly explore the $q_{Si} < 2.4$ and identify the global minimum around $q_{Si} = 2$ despite this position being far from the initial training set (see Fig. 8(b)). This signals that the iterative Bayesian optimization is able to "learn" by itself that the global minimum of R_χ does not belong to the initial training set. Overall, these results strongly support the ability of our approach to yield optimal forcefield parameters regardless of the choice of the initial training set considered at the beginning of the parameterization.

4.2. Comparison of the ML-based forcefield with previous Buckingham potentials

Finally, we discuss how our new ML potential (i.e., that featuring the optimal degree of complexity) compares with select previous SiO_2 forcefields relying on the Buckingham form. Specifically, we focus on (i) the BKS potential [12], which presents the same complexity as our new ML potential but relies on a different parametrization method and (ii) the CHIK potential [14], which presents a higher complexity (i.e., as it comprises Si—Si energy terms).

Fig. 9 shows a comparison of the partial PDFs predicted by our new ML forcefield with those predicted by the BKS and CHIK potentials. The data are also compared with the reference ab initio partial PDFs. We observe that both the ML and CHIK potentials offer a clear improvement with respect to the classic BKS potential. Since the ML and BKS forcefield relies on the same formulation and same degree of complexity, these results clearly demonstrate the superiority of our ML-based parametrization method over that used for the BKS potential—-which relies on ab initio calculations performed on small SiO_4 clusters and the incorporation of some bulk properties during training [12]. On the other hand, we find that our new ML forcefield offers a slightly more accurate prediction of the partial PDFs as compared to the CHIK potential while relying on a lower number of parameters (i.e., lower complexity). This confirms once again that Si—Si interactions are not playing a critical role in governing the structure of glassy SiO_2 and that, in turn, using Si—Si interactions as free parameters during the training of the forcefield can result in some degree of overfitting.

Finally, we assess whether our new ML forcefield offers a good transferability to α-quartz—that is, whether it can properly describe the structure and stiffness of α-quartz without being explicitly trained for this system. To this end, we compute the unit cell parameters at 300 K and elastic constants at 0 K of α-quartz using our potential (see Table 4) and compare these values to available experimental data [28–30].

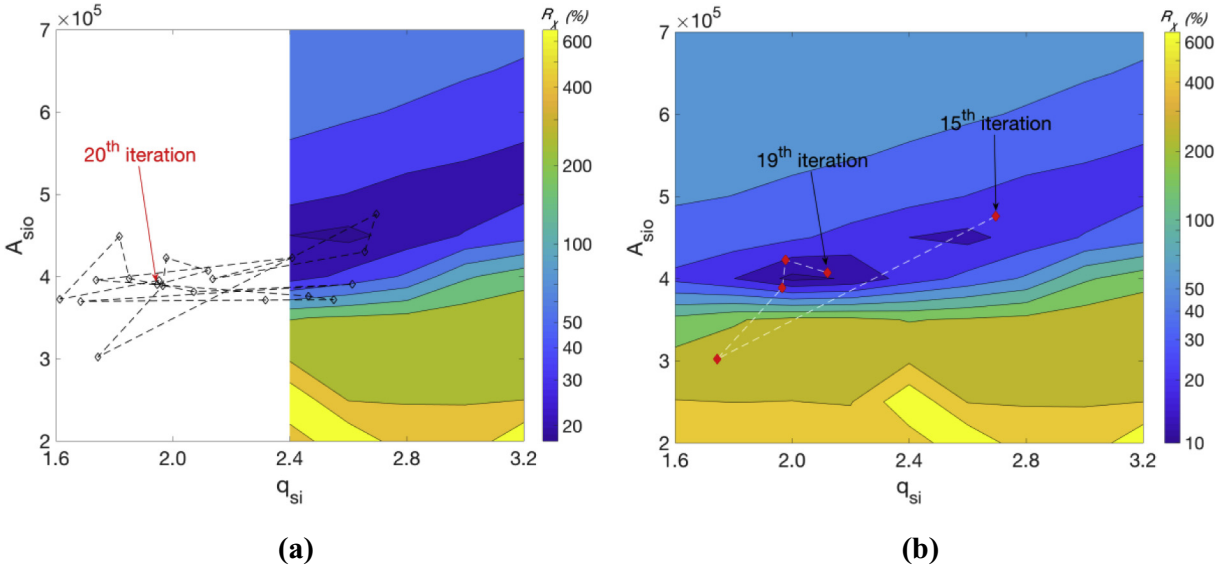

Fig. 8. Illustration of the iterative optimization approach used herein in the case of the global minimum is far from the initial training set. Only the partial charge of the Si atoms q_{Si} and the parameter A_{SiO} are here optimized, while the other 8 forcefield parameters are kept fixed. In both cases, the contour plot shows the value of the cost function R_χ as a function of q_{Si} and A_{SiO}. The white dashed line indicates the path explored by the Bayesian optimization method until the global minimum in the cost function R_χ is identified. Panel **(a)** highlight in white the parameter space region that is purposely excluded from the initial training set, while panel **(b)** shows the value of cost function over the entire domain to highlight the fact that the global minimum is indeed identified at the end of the optimization.

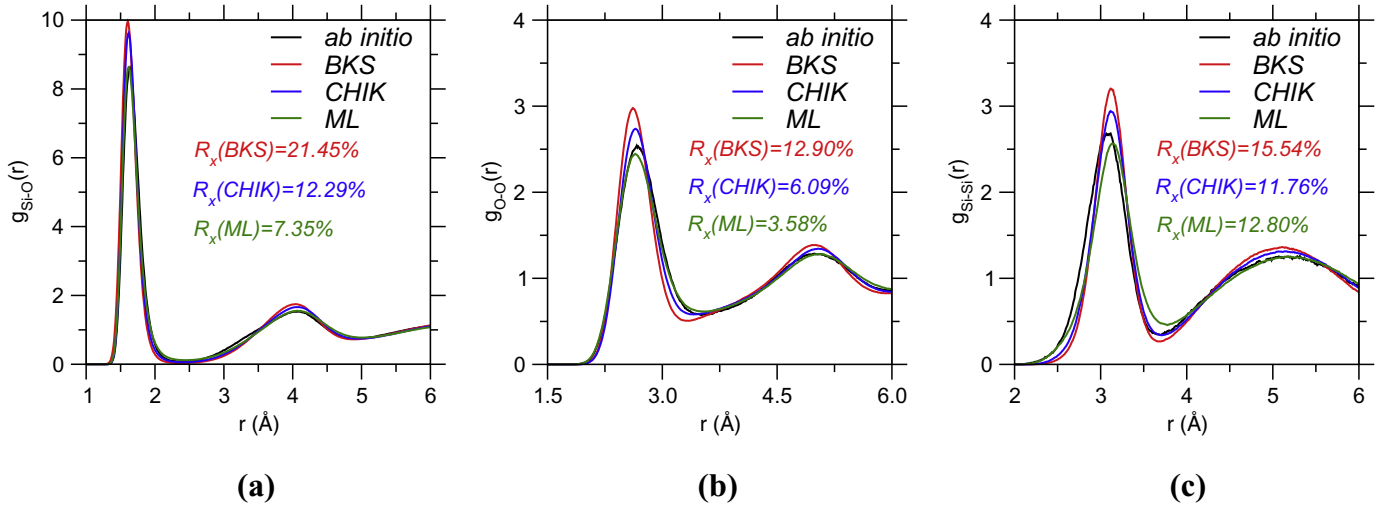

Fig. 9. **(a)** Si—O, **(b)** O—O, and **(c)** Si—Si partial pair distribution functions (PDFs) in liquid silica (at $T = 3600$ K) predicted by our new "ML" forcefield and compared with the ab initio reference [14]. The partial PDFs predicted by the BKS potential [12] and CHIK potential [14] are added for comparison.

Table 4
Unit cell parameters and elastic constants of α-quartz measured by experiments and offered by different Buckingham potentials.

Observable	Experiments [28–30]	BKS	CHIK	ML
V(Å^3)	112.93	119.30 ± 0.06	125.18 ± 0.05	128.8 ± 0.3
a (Å)	4.9124	5.026 ± 0.001	5.1166 ± 0.0008	5.1593 ± 0.0007
c (Å)	5.4039	5.4526 ± 0.0006	5.5212 ± 0.0006	5.5862 ± 0.0005
C_{11} (GPa)	86.8	90.9 ± 3.1	98.4 ± 0.6	89.2 ± 5.6
C_{33} (GPa)	105.8	116.3 ± 0.6	91.1 ± 0.9	67.0 ± 4.3
C_{44} (GPa)	58.2	48.6 ± 0.9	50.3 ± 0.5	46.1 ± 0.4
C_{66} (GPa)	39.9	46.0 ± 0.6	43.7 ± 1.1	23.9 ± 4.5
C_{12} (GPa)	7.0	−4.0 ± 1.3	−0.2 ± 0.7	−2.8 ± 9.3
C_{13} (GPa)	19.1	12.8 ± 0.3	16.8 ± 0.9	8.7 ± 3.6
C_{14} (GPa)	−18.0	−0.3 ± 0.1	−0.1 ± 0.2	−0.3 ± 1.0

These data are also compared with the values offered by the BKS and CHIK potentials. Overall, we find that our potential reproduces experimental data with a degree of accuracy that is comparable to that offered by previous potentials based on the Buckingham formulation (i.e., BKS and CHIK). This is notable as (i) α-quartz is not part of the training set used for the present ML forcefield and (ii) our forcefield was not explicitly trained to reproduce any stiffness data. This demonstrates that the pair distribution function (used to train the ML forcefield) contains enough details about the simulated system to offer a realistic description of the curvature of the interatomic potential (which largely controls stiffness). More generally, this shows that our new ML potential shows a satisfactory transferability to new phases (i.e., α-quartz) that are not explicitly considered during training.

5. Conclusions

Overall, this study establishes a general and versatile framework to facilitate the development of accurate, yet transferable empirical forcefields for the modeling of disordered materials. By taking the example of silica, our method is able to quickly parameterize forcefields featuring different degrees of complexity in a non-biased fashion. This robust method allows us to meaningfully assess the optimal degree of complexity for the forcefield, that is, for which an optimal balance between accuracy and simplicity is achieved. The assessment of the role of the complexity of forcefields is key to avoid any overfitting, which would likely decrease the transferability of the potential to new systems that are not explicitly included during training. More generally, we expect that the use of ML will decrease the importance of intuition for the parametrization of future potentials for multicomponent silicate glasses.

Acknowledgments

This work was supported by the National Science Foundation under Grants No. 1562066, 1762292, and 1826420.

References

[1] L. Huang, J. Kieffer, Challenges in modeling mixed ionic-covalent glass formers, in: C. Massobrio, J. Du, M. Bernasconi, P.S. Salmon (Eds.), Molecular Dynamics Simulations of Disordered Materials: From Network Glasses to Phase-Change Memory Alloys, Springer International Publishing, Cham, 2015, pp. 87–112, , https://doi.org/10.1007/978-3-319-15675-0_4.
[2] J. Du, Challenges in molecular dynamics simulations of multicomponent oxide glasses, in: C. Massobrio, J. Du, M. Bernasconi, P.S. Salmon (Eds.), Molecular Dynamics Simulations of Disordered Materials, Springer International Publishing, 2015, pp. 157–180.
[3] A.C.T. van Duin, S. Dasgupta, F. Lorant, W.A. Goddard, ReaxFF: a reactive force field for hydrocarbons, J. Phys. Chem. A 105 (2001) 9396–9409, https://doi.org/10.1021/jp004368u.
[4] Y. Yu, B. Wang, M. Wang, G. Sant, M. Bauchy, Revisiting silica with ReaxFF: towards improved predictions of glass structure and properties via reactive molecular dynamics, J. Non-Cryst. Solids 443 (2016) 148–154, https://doi.org/10.1016/j.jnoncrysol.2016.03.026.
[5] Y. Yu, B. Wang, M. Wang, G. Sant, M. Bauchy, Reactive molecular dynamics simulations of sodium silicate glasses — toward an improved understanding of the structure, Int. J. Appl. Glas. Sci. 8 (2017) 276–284, https://doi.org/10.1111/ijag.12248.
[6] M. Wang, N.M. Anoop Krishnan, B. Wang, M.M. Smedskjaer, J.C. Mauro, M. Bauchy, A new transferable interatomic potential for molecular dynamics simulations of borosilicate glasses, J. Non-Cryst. Solids 498 (2018) 294–304, https://doi.org/10.1016/j.jnoncrysol.2018.04.063.
[7] L. Deng, J. Du, Development of boron oxide potentials for computer simulations of multicomponent oxide glasses, J. Am. Ceram. Soc. (2018) 1–24, https://doi.org/10.1111/jace.16082.
[8] X. Li, W. Song, K. Yang, N.M.A. Krishnan, B. Wang, M.M. Smedskjaer, J.C. Mauro, G. Sant, M. Balonis, M. Bauchy, Cooling rate effects in sodium silicate glasses:

bridging the gap between molecular dynamics simulations and experiments, J. Chem. Phys. 147 (2017) 074501, , https://doi.org/10.1063/1.4998611.
[9] J.M.D. Lane, Cooling rate and stress relaxation in silica melts and glasses via microsecond molecular dynamics, Phys. Rev. E 92 (2015), https://doi.org/10.1103/PhysRevE.92.012320.
[10] K. Vollmayr, W. Kob, K. Binder, Cooling-rate effects in amorphous silica: a computer-simulation study, Phys. Rev. B 54 (1996) 15808–15827, https://doi.org/10.1103/PhysRevB.54.15808.
[11] A. Carré, S. Ispas, J. Horbach, W. Kob, Developing empirical potentials from ab initio simulations: the case of amorphous silica, Comput. Mater. Sci. 124 (2016) 323–334, https://doi.org/10.1016/j.commatsci.2016.07.041.
[12] B.W.H. van Beest, G.J. Kramer, R.A. van Santen, Force fields for silicas and aluminophosphates based on *ab initio* calculations, Phys. Rev. Lett. 64 (1990) 1955–1958, https://doi.org/10.1103/PhysRevLett.64.1955.
[13] P. Ganster, M. Benoit, J.-M. Delaye, W. Kob, Structural and vibrational properties of a calcium aluminosilicate glass: classical force-fields vs. first-principles, Mol. Simul. 33 (2007) 1093–1103, https://doi.org/10.1080/08927020701541006.
[14] A. Carré, J. Horbach, S. Ispas, W. Kob, New fitting scheme to obtain effective potential from Car-Parrinello molecular-dynamics simulations: application to silica, EPL. 82 (2008) 17001, , https://doi.org/10.1209/0295-5075/82/17001.
[15] S. Sundararaman, L. Huang, S. Ispas, W. Kob, New optimization scheme to obtain interaction potentials for oxide glasses, J. Chem. Phys. 148 (2018) 194504, , https://doi.org/10.1063/1.5023707.
[16] J.R. Shewchuk, An Introduction to the Conjugate Gradient Method Without the Agonizing Pain, Carnegie Mellon University, 1994.
[17] C.J. Fennell, J.D. Gezelter, Is the Ewald summation still necessary? Pairwise alternatives to the accepted standard for long-range electrostatics, J. Chem. Phys. 124 (2006) 234104, , https://doi.org/10.1063/1.2206581.
[18] A.C. Wright, The comparison of molecular dynamics simulations with diffraction experiments, J. Non-Cryst. Solids 159 (1993) 264–268, https://doi.org/10.1016/0022-3093(93)90232-M.
[19] J.-P. Hansen, I.R. McDonald, Theory of Simple Liquids: With Applications to Soft Matter, Academic Press, 2013.
[20] R. Car, M. Parrinello, Unified approach for molecular dynamics and density-functional theory, Phys. Rev. Lett. 55 (1985) 2471–2474, https://doi.org/10.1103/PhysRevLett.55.2471.
[21] N.P. Bansal, R.H. Doremus, Handbook of Glass Properties, Elsevier, 2013.
[22] P. Ganster, M. Benoit, W. Kob, J.-M. Delaye, Structural properties of a calcium aluminosilicate glass from molecular-dynamics simulations: a finite size effects study, J. Chem. Phys. 120 (2004) 10172–10181, https://doi.org/10.1063/1.1724815.
[23] P.I. Frazier, J. Wang, Bayesian optimization for materials design, Information Science for Materials Discovery and Design, Springer, Cham, 2016, pp. 45–75, , https://doi.org/10.1007/978-3-319-23871-5_3.
[24] C.E. Rasmussen, C.K.I. Williams, Gaussian Processes for Machine Learning, MIT Press, Cambridge, 2008.
[25] Y.L. Tong, The Multivariate Normal Distribution, Springer-Verlag, New York, 1990.
[26] H. Liu, Z. Fu, K. Yang, X. Xu, M. Bauchy, Parameterization of Empirical Forcefields for Glassy Silica Using Machine Learning, MRS Communications, (2019).
[27] B. Wang, Y. Yu, Y.J. Lee, M. Bauchy, Intrinsic nano-ductility of glasses: the critical role of composition, Front. Mater. 2 (2015) 11, , https://doi.org/10.3389/fmats.2015.00011.
[28] G. Will, M. Bellotto, W. Parrish, M. Hart, Crystal structures of quartz and magnesium germanate by profile analysis of synchrotron-radiation high-resolution powder data, J. Appl. Crystallogr. 21 (1988) 182–191, https://doi.org/10.1107/S0021889887011567.
[29] L. Levien, C.T. Prewitt, D.J. Weidner, Structure and elastic properties of quartz at pressure, Am. Mineral. 65 (1980) 920–930.
[30] H.J. McSkimin, P. Andreatch, R.N. Thurston, Elastic moduli of quartz versus hydrostatic pressure at 25° and −195.8°C, J. Appl. Phys. 36 (1965) 1624–1632, https://doi.org/10.1063/1.1703099.